Aerospace Science and Technology 127 (2022) 107708

Contents lists available at ScienceDirect

Aerospace Science and Technology

www.elsevier.com/locate/aescte

Sloshing reduced-order model based on neural networks for aeroelastic analyses

Francesco Saltari [a,*], Marco Pizzoli [a], Francesco Gambioli [b], Christina Jetzschmann [c], Franco Mastroddi [a]

[a] University of Rome "La Sapienza", Dept. of Mechanical and Aerospace Engineering, Via di Eudossiana 18, 00184 Rome, Italy
[b] Loads & Aeroelastics Dept., Airbus Operation Ltd, Filton, Bristol BS34 7PA, United Kingdom
[c] Functional Avionics Eng. & GNC Bremen, Airbus Defense & Space GmbH, Airbus Allee 1, 28199 Bremen, Germany

ARTICLE INFO

Article history:
Received 14 February 2022
Received in revised form 18 May 2022
Accepted 12 June 2022
Available online 20 June 2022
Communicated by Damiano Casalino

Keywords:
Nonlinear vertical sloshing
Reduced order models
Aeroelastic response
Neural networks

ABSTRACT

A thorough understanding of the effects of sloshing on aircraft dynamic loads is of great relevance for the future design of flexible aircraft to be able to reduce their structural mass and environmental impact. Indeed, the high vertical accelerations caused by the vibrations of the structure can lead to the fragmentation of the fuel free surface. Fluid impacts on the tank ceiling are potentially a new source of damping for the structure that has hardly been considered before when computing the dynamic loads of the wings. This work aims at applying recently developed reduced-order models of sloshing to the case of a research wing to investigate their effects on the wing aeroelastic response under pre-critical and post-critical conditions. The vertical sloshing dynamics is considered using neural networks trained with experimental data from a scaled tank and then integrated into the aeroelastic system following a suitable scaling procedure. The results concern the aeroelastic response of the wing to gust input under pre-critical (flutter) conditions as well as post-critical conditions highlighting the onset of limit cycle oscillations caused by sloshing, the only nonlinear phenomenon modelled in the present simulation framework. Moreover, the load alleviation performances will be assessed for a typical landing input.

1. Introduction

Vertical sloshing is a phenomenon that typically occurs in aeronautical structures when subjected to strong vertical accelerations. These structures withstand loads caused by gusts, turbulence, and landing impacts. The sloshing of fuel caused by vertical acceleration is coupled to the structural dynamics and aeroelasticity of the aircraft. It is well known that this type of sloshing leads to a noticeable increase in structural damping, yet it is generally not modelled in the design phase of modern aircraft. This work is part of the research activities within the European H2020 SLOshing Wing Dynamics (SLOWD) project and aims to provide reduced order models (ROMs) for the study of sloshing dynamics (Ref. [1]).

Vertical sloshing dynamics is one of the possible dynamics of the fluid stowed in the tanks, which has different characteristics compared to the classical sloshing that generally occurs during rotations and lateral motion of the tank. The latter generates standing waves inside the cavity, which provide dynamic coupling with the structure and a possible modification of flutter margins. In particular, the effects of sloshing on the aeroelastic flutter stability of aircraft have been discussed in Refs. [2–4] where sloshing dynamics was modelled using equivalent mechanical models (EMMs), frozen fluids and linear frequency domain approaches. Furthermore, the effects of sloshing on aeroelastic typical section behaviour have been investigated in Refs. [5,6] by direct time-marching analysis employing Smoothed Particle Hydrodynamics (SPH).

On the other hand, the subject of this paper is the sloshing phenomenon induced by a high vertical acceleration of the tank, that is, perpendicular to the free surface. As long as the vertical acceleration of the tank is kept below a certain threshold, the free surface does not break. However, exceeding this acceleration threshold triggers Rayleigh-Taylor instabilities (Ref. [7]), which determine a chaotic flow regime with air/water mixing. Turbulence, impacts with the tank ceiling and continuous free surface generation cause additional dissipation of energy (Refs. [8,9]). The overall balance of elastic potential energy and fluid energy leads to a noticeable increase in the effective damping of the structural motion. Moreover, when vertical harmonic motions are considered, it is noticed that the dissipative properties depend on the amplitude

* Corresponding author.
E-mail address: francesco.saltari@uniroma1.it (F. Saltari).

https://doi.org/10.1016/j.ast.2022.107708
1270-9638/

of the motion and the frequency. Ref. [10] experimentally investigated the dissipative behaviour of vertical sloshing considering a small-sized tank using an electromechanical shaker and evaluated the dissipated energy exploiting the definition of the hysteresis cycle.

Aeroelastic studies in which sloshing was modelled via the so-called *bouncing ball* ROM can be found in Ref. [11] where the damping performance of the aeroelastic/sloshing system was characterised as gust speed and intensity varied. More specifically, an equivalent mechanical model of bouncing ball was used to emulate the fluid behaviour inside the tank (the impacts with the tank wall). Indeed, classical sloshing ROMs are intrinsically based on potential fluid theory or small lateral perturbations [12–15] and, the identification of impulsive forces that vertical sloshing dynamics provides is not covered by these models. These new sloshing models - based on bouncing ball - address the need to describe this complex phenomenon through a simple physical model quickly and effectively. However, they suffer in being able to characterise well the dissipative capacity of the fluid at different values of amplitude and frequency as can be seen by comparing the energy maps provided in Refs. [10,16].

On the other hand, this work exploits the approach recently introduced in Ref. [16] for the generation of neural-network based ROM for vertical sloshing, by employing low-fidelity data and finally improved and experimentally validated for a *sloshing* beam in Ref. [17]. The use of neural network is getting attention in providing ROMs for fluid structure interaction (FSI) as it was already done for external aerodynamics in Ref. [18]. Artificial neural network can be seen as a parallel distributed processors made up of the so called neurons: simple processing units, having the natural capability of storing accumulated knowledge, and then, make it available for subsequent use. In particular, knowledge is acquired by the network from its environment through a *learning process*, and then stored by synaptic weights. Due to their useful properties and capabilities (Ref. [19]), neural networks are increasingly used in nonlinear system identification. Indeed, they are a powerful tool for approximating nonlinear dynamic systems, even when the structure of the system to be identified is unknown and only input–output data are available, so allowing a sort of generalised black-box modelling. Specifically, the sloshing forces will be estimated on the basis of the time series of the unsteady boundary conditions applied by the moving rigid tank. A Nonlinear Finite Impulse Response (NFIR) network is trained with an appropriate data series (consisting of vertical velocity of the tank and forces) obtained by a suitable scaled experiment (see Ref. [10]) spanning different values of *frequencies* and *displacement amplitude* in order to provide a nonlinear overall characterisation of fluid dissipation and fluid inertial behaviour.

Since the reduced-order model was obtained from data derived from a scaled model, an appropriate strategy for model scaling is then required. The full-scale models (one for each tank integrated into the wing) are based on the assumption that Froude number is the most characteristic of the non-dimensional parameters of vertical sloshing, whereas tank height is typically the characteristic length for this kind of sloshing. This assumption neglects the effects that fluid properties such as surface tension and viscosity have on free surface fragmentation by focusing on sloshing forces generated by fluid impacts within the tank.

A classic approach is used to model the rest of the aeroelastic system, *i.e.*, by employing the finite element method (FEM) to model the structure and the doublet lattice method (DLM) for the unsteady aerodynamics (see Ref. [20]). The aeroelastic analysis is based on the modes of vibration of the dry structure. A rational polynomial function approximation is applied to achieve a purely differential expression for the unsteady aerodynamics with the cost of defining a new set of aerodynamic finite states (see Refs. [21,22]). The nonlinear sloshing dynamics is then integrated into linear aeroelastic system. Response analyses under pre- and post-critical aeroelastic conditions illustrate how the sloshing dynamics helps to alleviate the dynamic loads following severe gusts while providing limit cycle oscillation beyond the flutter margin. Indeed, the characterisation of the limit cycle bifurcation provides results in line with those originally presented in Refs. [23,24] for a simplified aeroelastic model in wind tunnel.

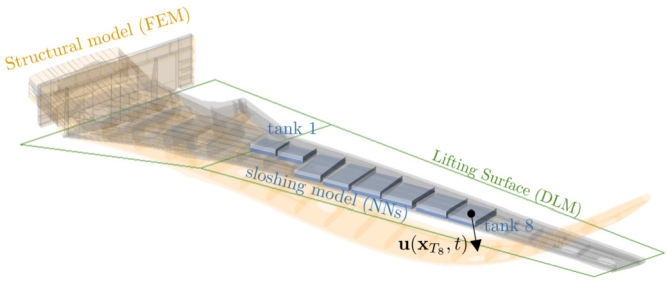

Fig. 1. Research wing aeroelastic/sloshing modelling.

Following the procedure applied for the gust analyses, the dynamic response of the wing to an operational landing impact is considered to assess the influence of the sloshing induced damping to alleviate landing loads.

The paper is organised as follows: the aeroelastic and sloshing modelling are introduced in Sec. 2, whereas the NN-based ROM is introduced in Sec. 3 along with the scaling procedure and the integration of the sloshing ROMs into the aeroelastic system. The aeroelastic response results are shown in Sec. 4. Finally, a section of concluding remarks ends the paper.

2. Aeroelastic and sloshing modelling

A sloshing/aeroelastic wing is modelled in this work using a hybrid model that combines a linear differential problem (aeroelasticity) with a data-driven model (sloshing). More in details, the numerical testbed is represented by a prototype wing model with dimensions typical of a single-aisle commercial aircraft wing. Fig. 1 shows the finite element model, along with the lifting surface discretized by means of doublet lattice method, and the position of the eight tanks integrated within the wing box. Fig. 2 shows the wing first six modes of vibration in the case of *dry* structure, that is the case in which tanks are empty, along with the corresponding natural frequencies normalized with respect to the first modal frequency ω_1. Dry modes are assumed to be the shape functions in order to avoid considering different FEM models depending on the fill level (even though the case with 50% fill level is considered in the present analysis). A box-shaped, rigid structure is approximated for each of the eight tanks embedded within the wing-box. Their dynamic behaviour is condensed in a point placed in the geometric centre of the tank and their motion is based on a weighted average of the motion of the surrounding nodes.

The wing structural displacements $\mathbf{u}(\mathbf{x}, t)$ can be expressed by the spectral decomposition

$$\mathbf{u}(\mathbf{x}, t) \simeq \sum_{n=1}^{N} \boldsymbol{\psi}_n(\mathbf{x}) q_n(t) \tag{1}$$

where $\boldsymbol{\psi}_n(\mathbf{x})$ are the modes of vibrations of the structure and $q_n(t)$ are the generalised coordinates describing the body deformation in time. Note that a space-discretisation for the structure is assumed by including a finite number N of modes in the analysis, *i.e.,* a frequency-band-limited unsteady process. Considering this representation for aircraft wing dynamics, one has the following Lagrange equations of motion in terms of N modal coordinates $q_n(t)$

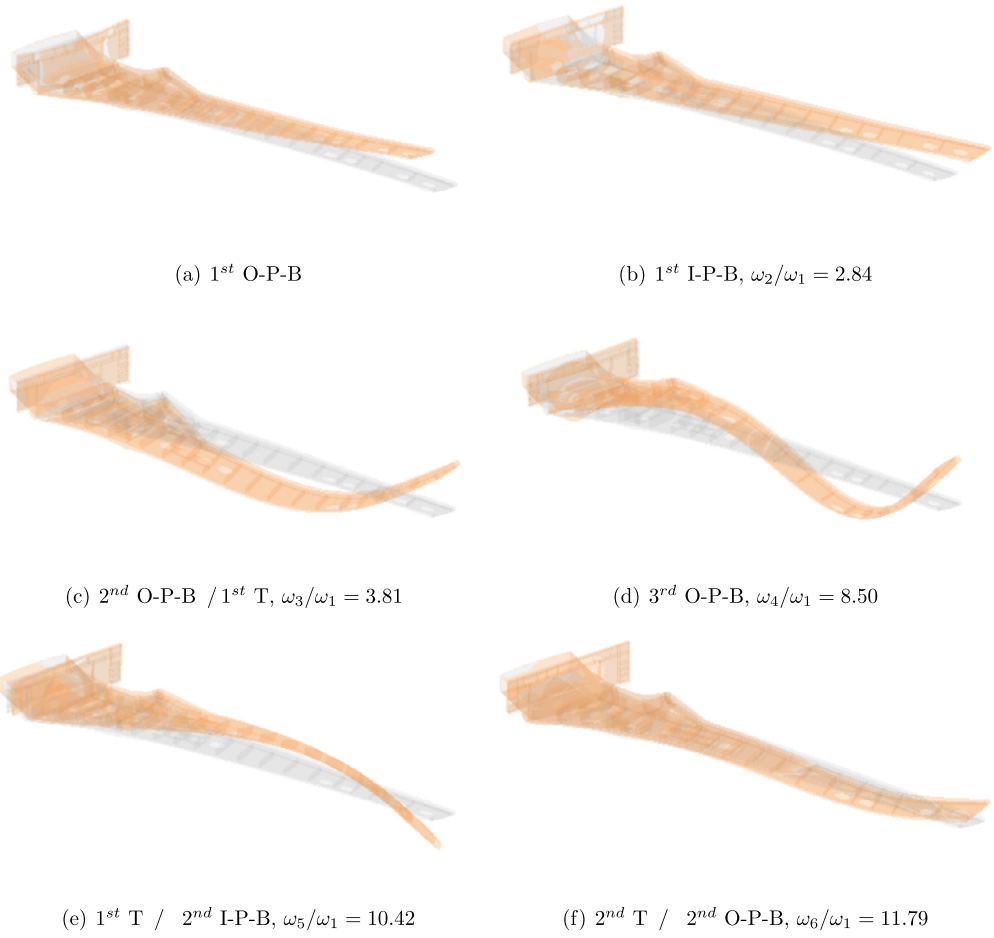

(a) 1^{st} O-P-B (b) 1^{st} I-P-B, $\omega_2/\omega_1 = 2.84$

(c) 2^{nd} O-P-B $/\,1^{st}$ T, $\omega_3/\omega_1 = 3.81$ (d) 3^{rd} O-P-B, $\omega_4/\omega_1 = 8.50$

(e) 1^{st} T $/$ 2^{nd} I-P-B, $\omega_5/\omega_1 = 10.42$ (f) 2^{nd} T $/$ 2^{nd} O-P-B, $\omega_6/\omega_1 = 11.79$

Fig. 2. Mode shapes of the wing model with their natural frequencies. O-P-B = Out-of-plane bending mode, I-P-B = In plane bending mode, T = torsional mode.

$$\mathsf{M}\ddot{\mathsf{q}} + \mathsf{K}\mathsf{q} = \mathsf{e} + \mathsf{g} + \mathsf{f}^{(ext)} \tag{2}$$

where $\mathsf{q} = [q_1, q_2, \ldots, q_N]^{\mathrm{T}}$ is the modal coordinates vector, M and K are, respectively, the modal mass and stiffness (diagonal) matrices provided by FEM solver, whereas $\mathsf{e} = [e_1, e_2, \ldots, e_N]^{\mathrm{T}}$ and $\mathsf{g} = [g_1, g_2, \ldots, g_N]^{\mathrm{T}}$ are, respectively, the generalised *aerodynamic* and *sloshing* forces induced by the elastic motion. The $\mathsf{f}^{(ext)}$ is the vector of the current external forcing terms which includes gust and landing force. The generalised aerodynamic forces (due to the aircraft motion only) are generally computed as a function of the reduced frequency $k = \omega b/U_\infty$ (with b semi-chord and U_∞ free stream velocity) and Mach M_∞ domain (see Ref. [20]) as:

$$\tilde{\mathsf{e}} = q_D\, \mathsf{Q}(k, M_\infty)\, \tilde{\mathsf{q}} \tag{3}$$

where $\mathsf{Q}(k, M_\infty)$ is the generalised aerodynamic forces matrix, q_D is the dynamic pressure and the symbol $\tilde{}$ is used to represent the Laplace/Fourier transforms. For a fixed value of M_∞, the following rational function approximation for the unsteady aerodynamics

$$\mathsf{Q}(k) \approx \mathsf{A}_0 + jk\mathsf{A}_1 - k^2\mathsf{A}_2 + jk\mathsf{C}\Big(jk\mathsf{I} + \mathsf{P}\Big)^{-1}\mathsf{B} \tag{4}$$

As a consequence of the rational function approximation, the aerodynamic forces can be recast in time domain as:

$$\mathsf{e} = q_D\, \mathsf{A}_0\, \mathsf{q} + q_D\, \frac{b}{U_\infty}\, \mathsf{A}_1\, \dot{\mathsf{q}} + q_D (\frac{b}{U_\infty})^2\, \mathsf{A}_2\, \ddot{\mathsf{q}} + q_D\, \mathsf{C}\, \mathsf{r} \tag{5}$$

$$\dot{\mathsf{r}} = \frac{U_\infty}{b}\, \mathsf{P}\, \mathsf{r} + \mathsf{B}\, \dot{\mathsf{q}} \tag{6}$$

where b is the reference half-chord and r is the vector of the aerodynamic finite states.

At the same time, the generalised sloshing forces vector g can be expressed as a sum of contributions $\mathsf{g}^{(i)}$ of individual tanks:

$$\mathsf{g} = \sum_{i=1}^{N_T} \mathsf{g}^{(i)} \tag{7}$$

with N_T the number of tanks. The *n-th* component of $\mathsf{g}^{(i)}$ is the projection of the fluid pressure distribution p_S evaluated on the wet tank surface $\mathcal{S}^{(i)}_{tank}$ on each *n-th* modal shape $\boldsymbol{\psi}_n$ as in the following ($\mathbf{n}$ unit normal vector to $\mathcal{S}^{(i)}_{tank}$)

$$g_n^{(i)} = -\oiint_{\mathcal{S}^{(i)}_{tank}} p_S\, \mathbf{n} \cdot \boldsymbol{\psi}_n\, d\mathcal{S} \tag{8}$$

By assuming a rigid tank identified by its geometrical centre, Eq. (8) can be recast as:

$$g_n^{(i)} = \mathbf{f}_S^{(i)} \cdot \boldsymbol{\psi}_n(\mathbf{x}_{T_i}) + \mathbf{m}_S^{(i)} \cdot \boldsymbol{\varphi}_n(\mathbf{x}_{T_i}) \tag{9}$$

where $\mathbf{f}_S$ and $\mathbf{m}_S$ are, respectively, the sloshing force and moment applied in the geometric centre of the tank $\mathbf{x}_{T_i}$, whereas $\boldsymbol{\varphi}_n(\mathbf{x}_{T_i})$ is the *n-th* modal rotation of the point $\mathbf{x}_{T_i}$. In this study, sloshing force is decomposed into two contributions: the inertial force according to the frozen fuel modelling (Ref. [3]) and the perturbation resulting from the relative motion of the fluid particles within the tank (Ref. [17]). Assuming there is only a vertical perturbation

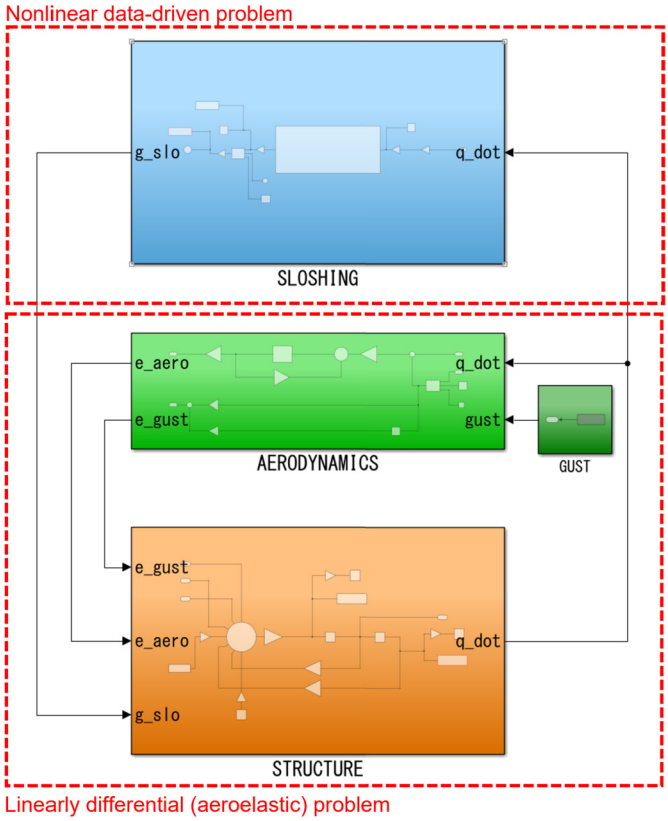

Fig. 3. Aeroelastic/sloshing modelling in Simulink®.

$\Delta f_{S_z}^{(i)}$, the sloshing force $\mathbf{f}_S$ and moment $\mathbf{m}_S$ about the geometric centre of the *i-th* tank are given by:

$$\mathbf{f}_S^{(i)} = -\sum_{k=1}^{N} m_l^{(i)} \left[\boldsymbol{\psi}_k(\mathbf{x}_{T_i}) - \mathbf{d} \times \boldsymbol{\varphi}_k(\mathbf{x}_{T_i})\right] \ddot{q}_k + \mathbf{i}_3 \Delta f_{S_z}^{(i)} \tag{10}$$

$$\mathbf{m}_S^{(i)} = -\sum_{k=1}^{N} \left(\mathbf{I}_l^{(i)} \boldsymbol{\varphi}_k(\mathbf{x}_{T_i}) - m_l^{(i)} \mathbf{d} \times \left[\boldsymbol{\psi}_k(\mathbf{x}_{T_i}) - \mathbf{d} \times \boldsymbol{\varphi}_k(\mathbf{x}_{T_i})\right]\right) \ddot{q}_k \tag{11}$$

where $\mathbf{d}$ is the offset between the geometric centre of the tank and the liquid centre of mass, $\mathbf{i}_3$ is the vertical unit vector and $\mathbf{I}_l$ is the inertia tensor of the frozen fluid. It is worth noting that $\Delta f_{S_z}^{(i)}$, hereafter denoted as *dynamic sloshing force* is a non-conservative force that is a nonlinear function of the history of the tank vertical displacement $u_z(\mathbf{x}_{T_i}, t)$. By considering Eqs. (10) and (11), Eq. (9) can be recast as:

$$g_n^{(i)} = -\Delta m_{nk}^{(i)} \ddot{q}_k + \mathbf{i}_3 \cdot \boldsymbol{\psi}_n(\mathbf{x}_{T_i}) \, \Delta f_{S_z}^{(i)} \tag{12}$$

where the components $\Delta m_{nk}^{(i)}$ provide a further non-diagonal contribution to the mass matrix given by the inertia of the fluid.

The aeroelastic/sloshing modelling is therefore implemented in Simulink® as illustrated in Fig. 3. The aeroelastic blocks are purely differential whereas the sloshing block is modelled with neural networks trained by means of data made available by experiments carried out with a small scale tank [17]. The description of such approach based on neural network to describe $\Delta f_{S_z}^{(i)}$ is covered in Sec. 3

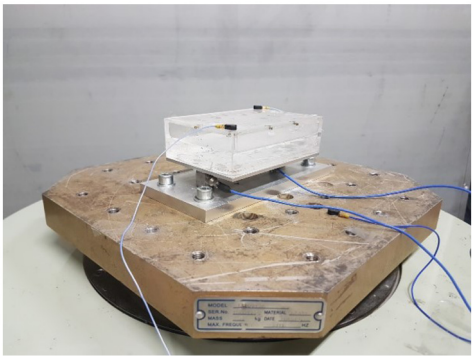

Fig. 4. Experimental layout.

3. Neural-network-based ROM of vertical sloshing

In this section the neural-network-based ROM is presented. The description of the experimental set-up used for the network generation is presented in Sec. 3.1, whereas the scaling procedure for obtaining the sloshing model for the actual application is presented in Sec. 3.2.

3.1. A neural-network based ROM from experiments

In this study, we use the same approach developed in Ref. [17] to generate a reduced order model based on neural networks used for investigating the effects of nonlinear sloshing on the response of the wing aeroelastic system. The model is identified by exploiting the experimental data obtained from the experimental setup depicted in Fig. 4. The experimental testbed is a box-shaped tank made in plexiglass with a height of $h = 27.2$ mm and base of sides $l_1 = 117.2$ mm and $l_2 = 78.0$ mm. The dimensions were chosen in order to be able to trigger slamming with the tank ceiling after the occurrence of the Rayleigh-Taylor instabilities. The tank was placed over a controlled electrodynamic shaker able to impose vertical sinusoidal displacement. The dynamic load at the interface between shaker and tank is measured by two load cells, placed in the middle of the long side of the tank base. The system is also equipped with two redundant accelerometers placed at the opposite corners of the tank upper closing side and with a control accelerometer used by the shaker controller. In Reference [10], this experimental set-up was exploited to investigate the dissipative behaviour of the fluid sloshing inside a tank set in vertical motion. Indeed, if one represents the fluid tank interface force as a function of the displacement, *e.g.* by using experimental measurements, one obtains in harmonic regime a hysteresis cycle with the closed area representing the energy dissipated L_d by the fluid in a cycle. Fig. 5(a) provides the non-dimensional energy dissipated by the sloshing fluid $\Phi_d = L_d/(m_l a^2 \Omega^2)$ in a vertical harmonic motion $u_z = a\cos(\Omega t)$ (with a displacement amplitude of the imposed motion and Ω the excitation frequency) as a function of the non-dimensional frequency $\bar{\omega} = \Omega/\sqrt{g/h}$ (not to be confused with the reduced frequency k for the unsteady aerodynamics) and velocity $\bar{v} = v/\sqrt{gh}$ (with $v = \Omega a$) that, for the vertical slosh dynamics assumes the meaning of Froude number (Ref. [25,26]). Moreover, for the same kind of input, the variation of the sloshing-effective mass fraction β (see Fig. 5(b)) can be identified by assuming the linear approximation of the dynamic sloshing force (removing the effects of the super-harmonics) and performing the ratio between the Fourier transform of the dynamic sloshing force and the related frozen mass force

$$\beta = \Re\left[\frac{\Delta\tilde{f}_{S_z}(\Omega)}{m_l\,\Omega^2\,\tilde{u}_z(\Omega)}\right] \tag{13}$$

where $\Re[\,]$ is used to express the real part. Appendix A provides analytical details and interpretation of this quantity. This effect, that will result critical in the aeroelastic response close to the flutter margin, was already investigated in Ref. [27]. A reference value $\hat{\beta} = -0.154$ is obtained by averaging among the experimental values obtained at low level of acceleration ($0.25g$), namely for the quasi-linear sloshing regime. Nonetheless, a small uncertainty in defining the exact amount of liquid in the tank during the experiment affects this value.

Subsequently, the experimental set-up was used to generate a data set for training a neural network by means of a 480 s long test with a variable frequency and amplitude harmonic imposed acceleration $\ddot{u}_z = f(t)\cos(\int \Omega(t)dt)$ such as to suitably cover the frequency-velocity domain of interest (see Fig. 6(a)). A different data set 240 s long covering the same points in the frequency-velocity domain is used for validation in order to avoid overfitting of training data. The acquired sensor measurements were used to train the neural network. More in detail, Fig. 6(b) shows the vertical velocity of the tank obtained by integrating the acceleration signal, that is the input feeding the network, whereas, the dynamic sloshing forces, estimated by the load cells subtracting the frozen fluid and tank masses inertia are shown in Fig. 7.

Among the wide variety of dynamical models, a Nonlinear Finite Impulse Response (NFIR) model has been considered (see Fig. 8). The output of the network, the dynamic sloshing force at a given time instant, is obtained by means of a static approximator that receives the recent time history of the tank vertical velocity as input. NFIR models, simply made up by static approximator and bank of filters with delay lines, generally ensures the stability of the network (Ref. [28]). The used NFIR model consists of 1 hidden layer with 20 neurons and 1 output layer whilst 60 tapped delay lines are considered for the input. Normalised radial basis functions are employed as activation functions in all nodes of the hidden layer, whereas the output layer is made up with a simple linear function. *Levenberg-Marquardt* backpropagation algorithm, implemented in Matlab® through the *trainlm* function (Ref. [29]), is used for the network training. The model identified in this study was trained using an error rate increase criterion over 6 consecutive epochs as the stopping criterion. The stopping of the training process occurred after 76 epochs, when the mean-squared error performance had already stabilised at a constant and relatively low value. The trained network was then converted into a Simulink® block to be used for simulations and thus obtaining predictions for the output. Fig. 9 shows the dynamic sloshing force (in red) that the network predicts when the tank is excited with the velocity time history of the validation data set compared to the validation sloshing force (in black). The identified network looks to be able to accurately describe the nonlinear behaviour of sloshing.

3.2. Scaling of the sloshing forces

More in general, the energy dissipated by the sloshing fluid L_d can be expressed by means of the π-theorem:

$$L_d = m_l a^2 \Omega^2 \Phi_d\,(\bar{\omega}, \bar{v}, \alpha, Re, Bo, \ldots) \tag{14}$$

Besides the non-dimensional frequency $\bar{\omega}$ and velocity $\bar{v}$, L_d is dependent on the fill level α, the Reynolds number $Re = vh/\nu$ (ν kinematic viscosity) that reflects viscosity effects, and the Bond number $Bo = \rho g h^2/\gamma$ (γ surface tension) that reflects surface tension effects. Since the operational parameters $\bar{\omega}$ and $\bar{v}$ only cover a subspace of the space spanned by the non-dimensional parameters influencing the sloshing-induced energy dissipation, it is necessary to formulate the following hypotheses before scaling the NN-based ROM:

- The non-dimensional dissipated energy is assumed to be mainly dependent on the non-dimensional velocity (Froude) and non-dimensional frequency. Other parameters more related to physical properties of the fluid (Reynolds and Bond) are assumed to play a secondary role.
- The principal dimension is assumed to be the tank height h (Ref. [25]). Tank base area is not assumed to be important.
- For each filling level α a different identification is required.

Although these hypotheses are only partially supported by experiments and numerical evidences [25,30], it is reasonable to assert them to scale the obtained data for the eight tanks embedded within the structure. Indeed, a variation in the dimensionless parameters of Reynolds (at high Reynolds values) and Bond seems to provide a negligible influence on the dissipative capabilities during violent vertical sloshing phenomena (Ref. [30]). The re-scaled ROM must therefore work in similarity of non-dimensional velocity and non-dimensional frequency as well as non-dimensional dissipated energy in order to replace the sloshing model with a neural network capable of reproducing the real dissipative behaviour. Fig. 10 shows the Simulink® implementation of the neural network unit and the scaling gain. More in details, from the non-dimensional frequency similarity between the experiment $\bar{\omega}^{(exp)}$ and the *i-th* tank $\bar{\omega}^{(i)}$, we obtain:

$$\frac{\Omega^{(exp)}}{\sqrt{g/h^{(exp)}}} = \frac{\Omega^{(i)}}{\sqrt{g/h^{(i)}}} \Longrightarrow dt^{(i)} = dt^{(exp)}\sqrt{\frac{h^{(i)}}{h^{(exp)}}} \tag{15}$$

Thus, a proper time rate translator is used within the simulation (see Fig. 10) to make the neural network working with a time rate compliant with the one used for its identification. Furthermore, the similarity of the non-dimensional velocity (Froude) of the vertical motion yields:

$$\frac{v^{(exp)}}{\sqrt{gh^{(exp)}}} = \frac{v^{(i)}}{\sqrt{gh^{(i)}}} \Longrightarrow v^{(i)} = v^{(exp)}\sqrt{\frac{h^{(i)}}{h^{(exp)}}} \tag{16}$$

that provides a gain to the vertical tank velocities before the call to the neural network (see Fig. 10). Assuming the similarity of the non-dimensional dissipative function Φ_d and that $L_d = \int_{cycle} \Delta f_{S_z} d\,u_z$ we obtain:

$$\Delta f_{S_z}^{(i)} = \Delta f_{S_z}^{(exp)} \frac{m_l^{(i)}}{m_l^{(exp)}} = \Delta f_{S_z}^{(exp)} \frac{\rho_k V^{(i)}}{\rho_w V^{(exp)}} \tag{17}$$

where ρ_k and ρ_w are the density of kerosone and water, respectively, whereas $V^{(i)}$ and $V^{(exp)}$ are the volume of the *i-th* wing tank and experimental tank, respectively. Equation (17) provides the gain for the dynamic sloshing forces to be applied after the call to the neural network within the simulation framework (see Fig. 10). This scaling procedure is able to take into account different liquids with respect to that used for data generation. In this scaling procedure, velocity and displacements of the tank are adjusted according to tank size, but the maximum accelerations achievable when the tank works in similarity with the tank used for the network identification are retained. It is worth noting how this scaling procedure assumes a perfectly box-shaped tank. In addition, the dependence of the dissipative characteristics of vertical sloshing with respect to aspect ratios (the other two dimensions of the tank with respect to its height) and wing dihedral angle has not yet been thoroughly investigated and are not considered in this work.

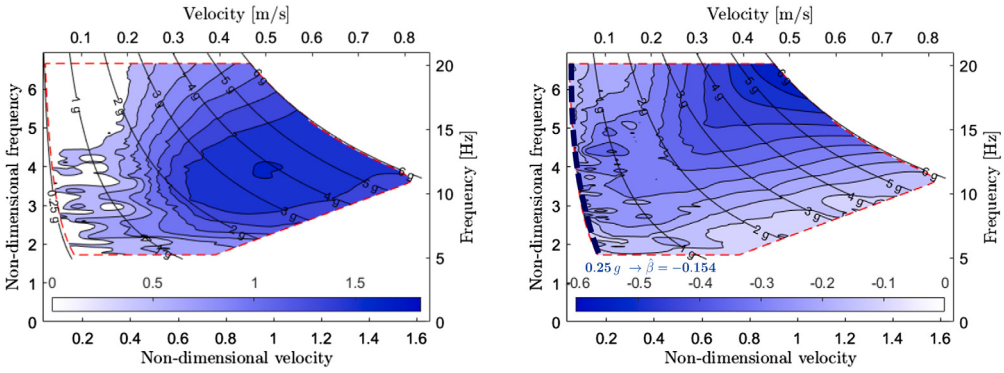

(a) Nondimensional dissipated energy Φ_d (b) sloshing-effective mass fraction β

Fig. 5. Maps of the Identified dissipated energy and sloshing-effective mass fraction.

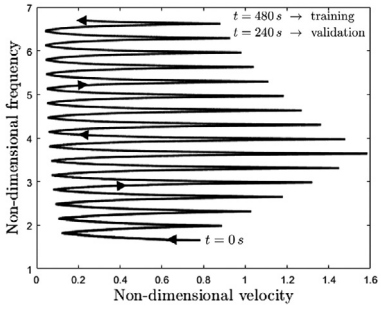

(a) Velocity path in non dimensional frequency-amplitude domain

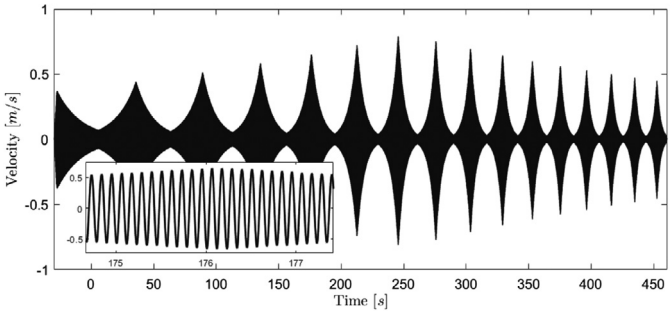

(b) Time history of the velocity for the training data set

Fig. 6. Velocity profile used to train the network, see Ref. [17].

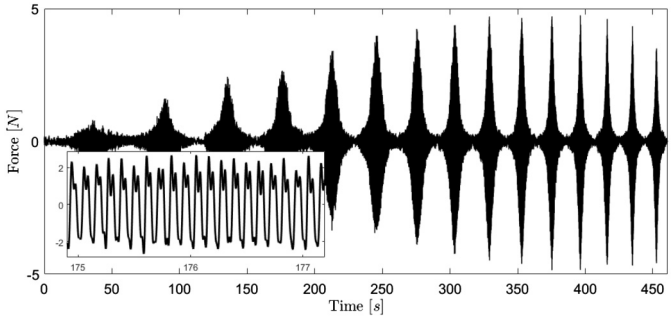

Fig. 7. Time history of the dynamic sloshing forces for the training data set.

4. Aeroelastic response analyses

Before performing the aeroelastic response of the wing, a stability analysis is performed by evaluating the poles of the linearised

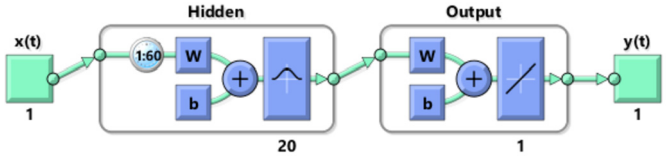

Fig. 8. Time-Delay Neural Network flowchart.

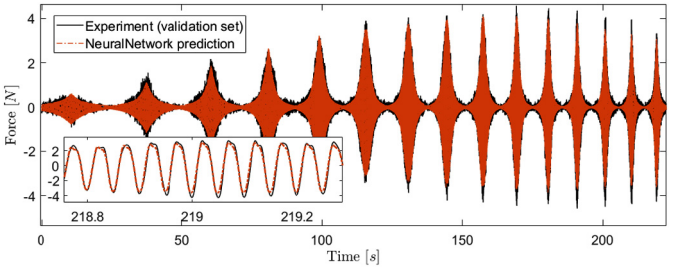

Fig. 9. Comparison between the output predicted by the identified neural network and the experimental time history of the force used for the training. (For interpretation of the colours in the figure(s), the reader is referred to the web version of this article.)

aeroelastic system between 250 m/s and 360 m/s and considering fixed the Mach number $M_\infty = 0.85$ and the air density $\rho_\infty = 0.9$ kg/m^3. Twelve vibration modes are employed for the aeroelastic analyses whereas 200 aerodynamic states were used for the rational function approximation of the unsteady aerodynamics. An additional modal damping of 5% is introduced into the analysis only for vibration modes whose dry nondimensional frequency with respect to the size of the wing bigger tank was greater than the nondimensional frequency limit of the sloshing identification process, namely when $f_n/\sqrt{g/h_1} > 6.72$. The root locus of the aeroelastic system (frozen configuration $\Delta f_{S_z}^{(i)} = 0$) is shown in Fig. 11 in which the vibration modes from which the different branches originate are annotated. The flutter instability occurs at $U_\infty = U_F = 319.3$ m/s from the branch that originates from the first bending mode (see Fig. 2(a)), whereas the flutter frequency is $\omega_F = 1.95\,\omega_1$. The critical mode mainly consists of a coupling between the first vibration mode (1st O-P-B) and the third mode (2nd O-P-B / 1st T) that consists also of a slight torsion of the aerodynamic sections. Moreover, Fig. 12 shows the trend of the flutter speed as a function of the filling level α, where the green square represents the speed value in the case a fuel mass correction is used to take into account the sloshing effective mass at small perturbances, namely by assuming

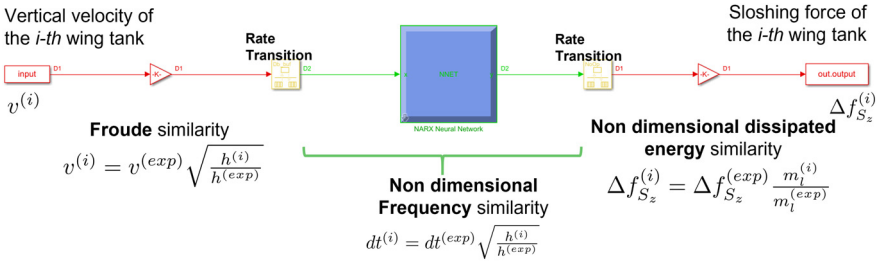

Fig. 10. Scaling procedure implemented in Simulink®.

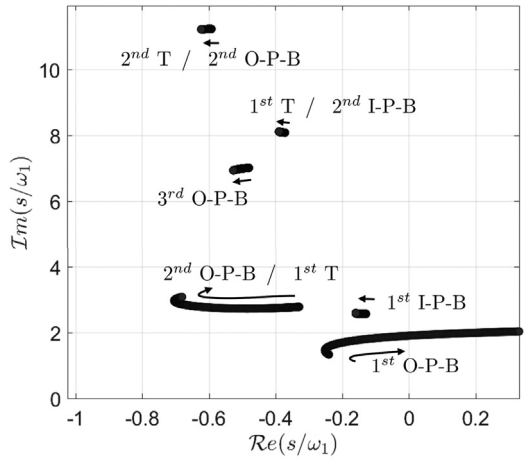

Fig. 11. Root Locus of the aeroelastic system.

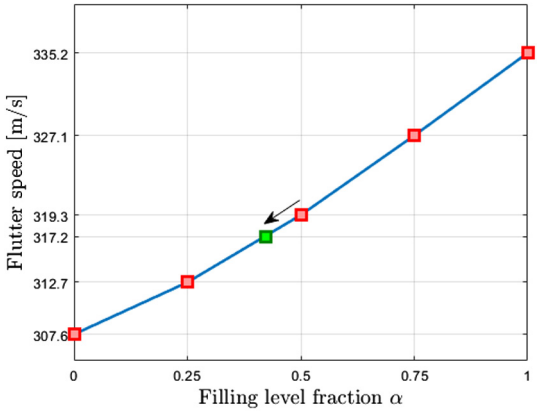

Fig. 12. Flutter speed as a function of the filling level fraction α.

$$\Delta f_{S_z}^{(i)} = \hat{\beta}\, m_l^{(i)} \sum_{n=1}^{N} \mathbf{i}_3 \cdot \boldsymbol{\psi}_n(\mathbf{x}_{T_i}) \ddot{q}_n \tag{18}$$

that can be integrated in Eq. (12).

Aeroelastic response analyses to vertical gust are then performed for different velocities in the neighbourhood of the flutter speed where the response is less damped and the sloshing may play a role of paramount relevance on damping aeroelastic vibrations. Since the neural network is trained considering a time history made of a sequence of simply-harmonic input with different frequency and amplitude values (see Fig. 6), it follows that the proposed sloshing model works consistently when the input velocity has a dominant harmonic. The external aerodynamics plays a key role on filtering a single mode that has a pole with a smaller real part making the proposed ROM suitable to study most of the aeroelastic response analyses (like the aeroelastic response to discrete gusts). Specifically, in this analysis we consider the following standard gust profile:

$$w_g(t) = \frac{1}{2} w_{g_a} \left(1 - \cos\left(\frac{2\pi U_\infty t}{L_g}\right)\right) \tag{19}$$

where w_{g_a} is the gust amplitude. The reference value for the gust length measured in chord length b is $L_g = 25\,b$. Spatially, the gust is assumed to be constant throughout the wing domain. Two models are compared, namely the *frozen fuel* model and the *sloshing fuel* model that employs the neural network to replace slosh dynamics. Three different flight conditions are considered, that is $U_\infty = 266$ m/s and $U_\infty = 315$ m/s, before the flutter margin as evaluated by the frozen fuel model, and $U_\infty = 321$ m/s in flutter condition. The gust amplitude w_{g_a} is assigned in order to do not make the vertical acceleration overcome the limit of $6\,g$ at the tank locations which would violate the range of applicability of the network. Different gust intensities are employed to highlight the increase of the sloshing induced damping at high response amplitudes or the onset of limit cycle oscillations.

The first analysis is performed at a free stream velocity of $U_\infty = 266$ m/s, with a gust intensity of $w_{g_a} = 6$ m/s. Fig. 13(a) compares the wing response of the sloshing fuel model with the frozen fuel model in terms of tip acceleration. Despite the aerodynamic damping is high, the role of sloshing is evident since the sloshing fuel model results in a more damped response due to presence of the fluid impacting inside the tanks. Moreover, the response of the dynamic sloshing forces, obtained by exploiting the neural network-based ROM, can be observed in Fig. 13(b).

Then, the flight speed is brought close to the flutter margin, at a free stream velocity of $U_\infty = 315$ m/s, with a gust intensity of $w_{g_a} = 3$ m/s. Fig. 14(a) compares the wing tip response of the sloshing fuel model with the frozen fuel model. Even though, the structure is closer to the flutter margin, it can be noticed how the beneficial influence of the damping introduced by sloshing dynamics helps to alleviate the gust response. Again, the response of the dynamic sloshing forces, obtained by exploiting the neural network-based ROM, can be observed in Fig. 14(b).

The post-critical gust response analysis is performed after the flutter speed limit evaluated with the frozen fuel model, that is $U_\infty = 321$ m/s, with a gust intensity of $w_{g_a} = 1.5$ m/s. The wing tip response is shown in Fig. 15(a) comparing the two considered cases. The linear frozen case results in a fluttering response with diverging exponential envelope, whilst the sloshing case develops a limit-cycle oscillation (LCO). This LCO is determined by the nature of the sloshing forces, which become highly dissipative when the acceleration of the tank increases (Rayleigh-Taylor instabilities occur above 1 g). Fig. 16 compares the response of the sloshing fuel model for two different gust amplitudes, that is $w_{g_a} = 0.15$ m/s and $w_{g_a} = 2.5$ m/s. Within the range of maximum allowable vertical acceleration at the tank locations (given by the identification process), the response of the wing converges to the same limit cycle oscillation.

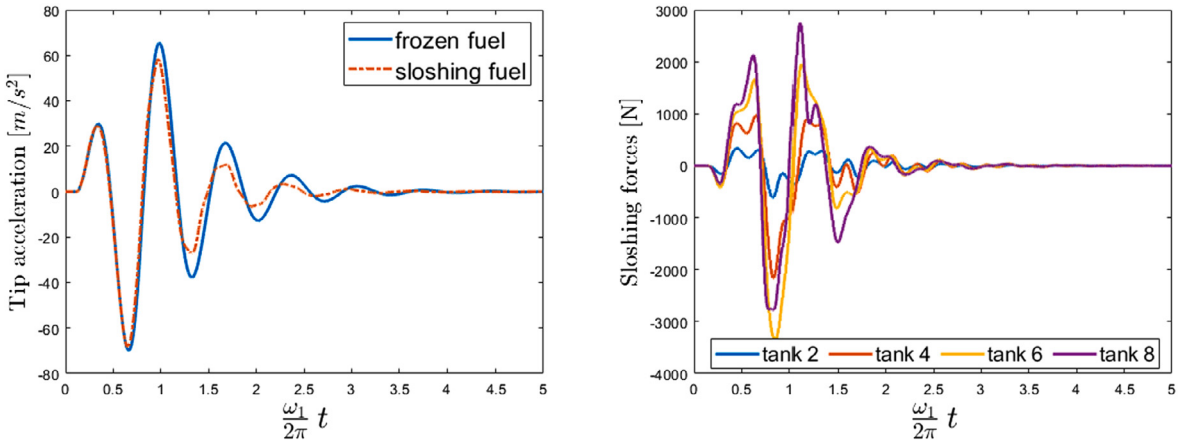

(a) Tip vertical acceleration (b) Dynamic sloshing forces

Fig. 13. Gust response analysis for $U_\infty = 266$ m/s.

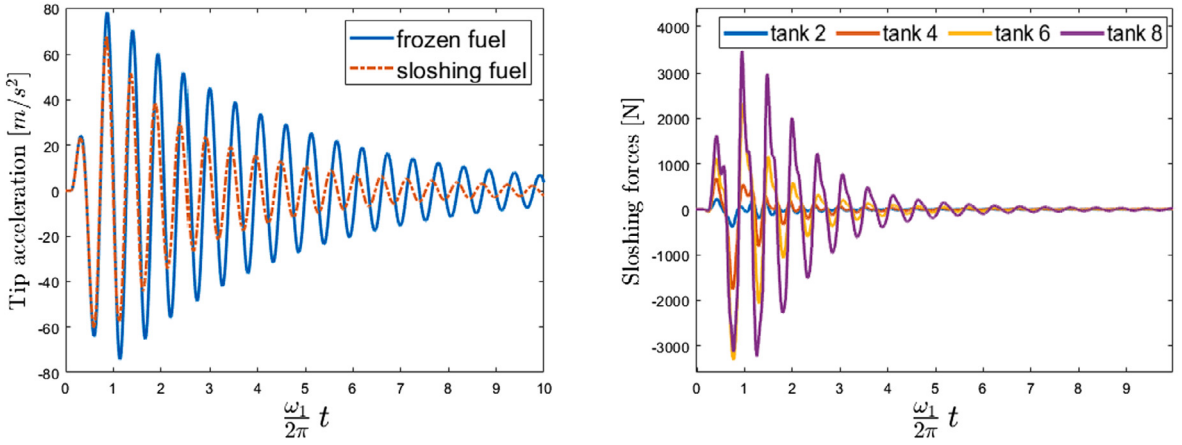

(a) Tip vertical acceleration (b) Dynamic sloshing forces

Fig. 14. Gust response analysis for $U_\infty = 315$ m/s.

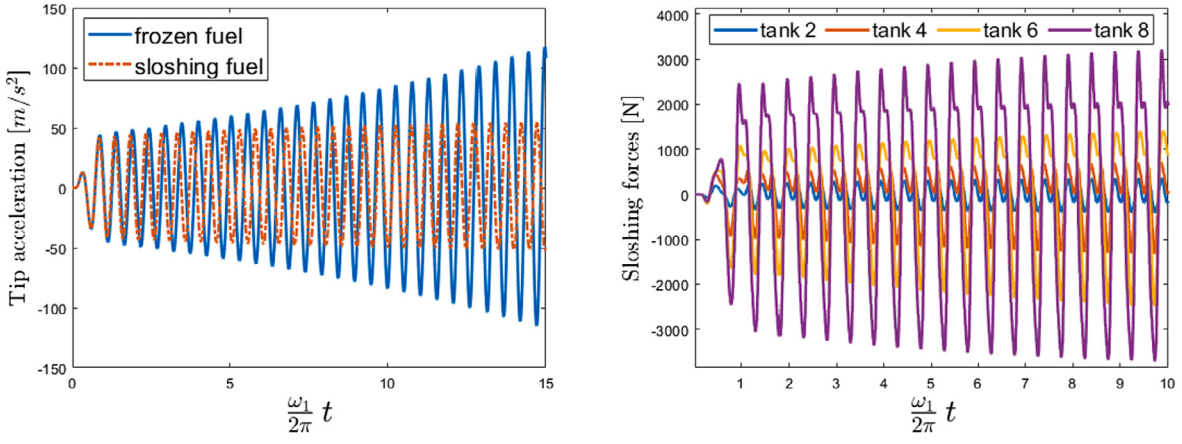

(a) Tip vertical acceleration (b) Dynamic sloshing forces

Fig. 15. Gust response analysis for $U_\infty = 321$ m/s.

More in general, the response analysis to small disturbances ($w_{g_a} = 0.15$ m/s) is carried out spanning from 316 m/s to 323 m/s. Fig. 17 shows the Hopf bifurcation diagram of the limit-cycle oscillation of the wing tip displacement. Despite the nonlinear stabilising contribution of the sloshing forces, the system is nevertheless unstable after a flight speed slightly lower 323 m/s. This denotes the presence of an unstable branch coexisting with the stable one identified by the numerical simulations. Moreover, because the sloshing forces are primarily dissipative, the unstable branch cannot exist before the flutter speed. It is worth not-

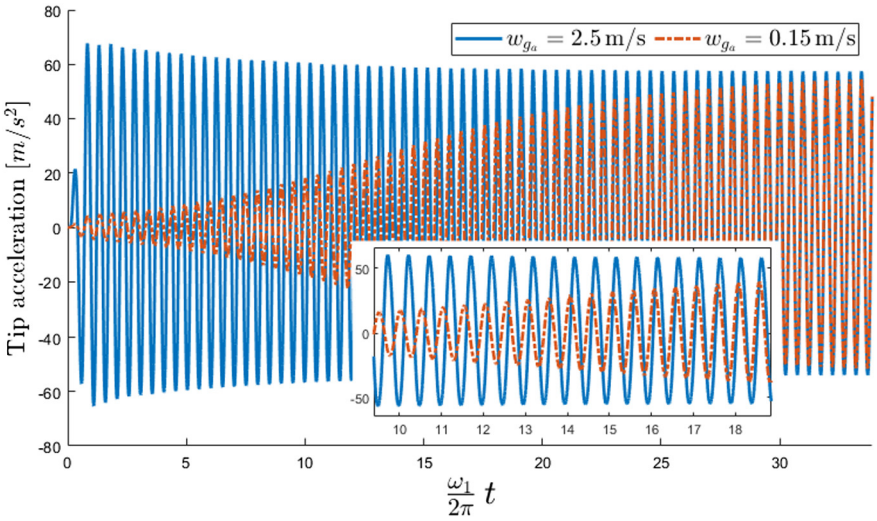

Fig. 16. Gust response analysis for $U_\infty = 321$ m/s considering two different gust amplitudes.

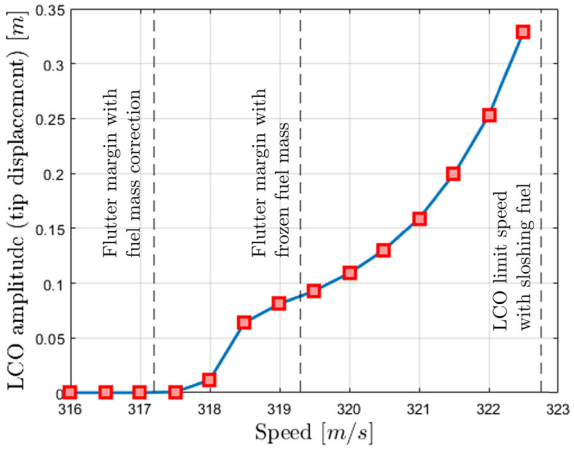

Fig. 17. Bifurcation diagram.

ing that the limit cycle oscillations of the stable branch exist in a range of displacement amplitude that generally structures of this type can withstand in terms of maximum allowable stresses. Moreover, sloshing is able to provide a limit cycle response up to a velocity which is slightly greater than the linear flutter speed. Therefore, for flutter analyses, this effect must be weighed against other uncertainties from structural and aerodynamic modelling.

Fig. 18(a) shows a contour plot of the energy exchanged between the structure and external aerodynamics per cycle as a function of the amplitude of the response and flight speed in case the response were solely determined by the unstable branch of the root locus in Fig. 11, or $\mathsf{q}(t) \approx \mathsf{w}_1 a_1(t) + c.c.$[1] The blue colour indicates the region in which the aerodynamics subtract energy from the structure (positive damping, stable), whereas the red-one indicates that the structure is absorbing energy from the aerodynamics (negative damping, flutter condition).

[1] From mode tracking we obtain the eigenvector $\mathsf{w}_{1_{track}}(U_\infty)$ corresponding to unstable branch as a function of the flight speed (that is normalised in order to have real and unit displacement at tip $\longrightarrow a_1$ assumes the meaning of the tip displacement) and the associated frequency $\omega_{1_{track}}(U_\infty)$. Therefore, the following quantity yields the energy exchanged by the structure and the external aerodynamics in a cycle with angular frequency $\omega_{1_{track}}$:

$$L_{aero}(U_\infty, a_1) = \pi\, a_1^2\, \frac{1}{2}\rho U_\infty^2\, \mathcal{I}\left\{\mathsf{w}_{1_{track}}^{\mathsf{T}}\, \mathsf{Q}\left(\frac{\omega_{1_{track}}\, b}{U_\infty}\right) \mathsf{w}_{1_{track}}\right\}. \tag{20}$$

On the other hand Fig. 18(b) provides the energy exchanged by the internal sloshing fluid with the structure summarising the effects of the eight tanks by dimensionalisation and the sum of the map in Fig. 5(a). This energy map, similarly to the one in Fig. 18(a), is based on the tracking of the critical eigenvector and frequency. By increasing the flight speed, the map is not defined at the higher amplitude because of the increase of the considered aeroelastic frequency. The dissipative nature of sloshing is thus highlighted (positive damping, stabilising effect).

The energy exchanged between the structure and the fluids (external aerodynamics and sloshing) can be computed by integrating the maps in Figs. 18(a) and 18(b) (see Fig. 18(c)). This figure is overlaid with the LCO bifurcation in Fig. 17. The zero-energy isoline should represent the locus of points at which fuel sloshing dissipates as much energy as the aerodynamics induces onto the structure, and thus represents the LCO bifurcation obtained directly from the energy map analysis [31]. Note that the LCO bifurcation identified by simulation is similar to the one obtained by energy consideration but it is shift of about 2 m/s due the inertial effects of the fluid in the tank that anticipate the onset of flutter (as shown in Fig. 17). Considering the dissipative nature of sloshing, the total energy exchanged between structure and fluid before the flutter speed will always result in positive damping. Moreover, as a result of the saturation of the dissipated energy, an unstable branch may result with vertical asymptote at flutter speed. This *a-priori* post-critical analysis based on energy maps shows that the neural-network-based ROM is capable to reproduce the behaviour of the slosh dynamics when integrated in a complex aeroelastic computational environment.

4.1. Landing response analysis

The last analysis is performed considering landing condition with a reference free stream velocity equal to $U_\infty = 150$ m/s and Mach $M_\infty = 0.43$. The simplified landing modelling is accounted in modal coordinates by specialising the external forces $\mathsf{f}^{(ext)}$ in Eq. (2):

$$\mathsf{f}^{(ext)} = \mathsf{b}\,\ddot{u}_{z_f} \tag{21}$$

where $\ddot{u}_{z_f}$ is the vertical acceleration of the fuselage and therefore of a system moving according with the wing. Moreover, the *n-th* component of the input vector b is obtained by:

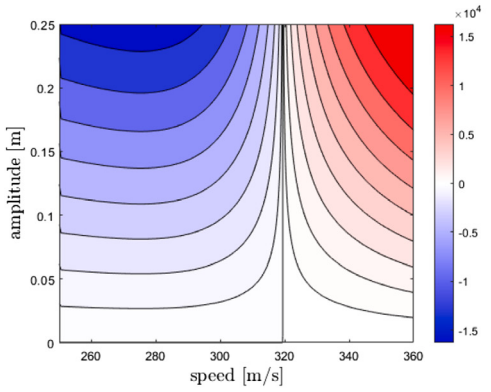

(a) Aeroelastic energy map

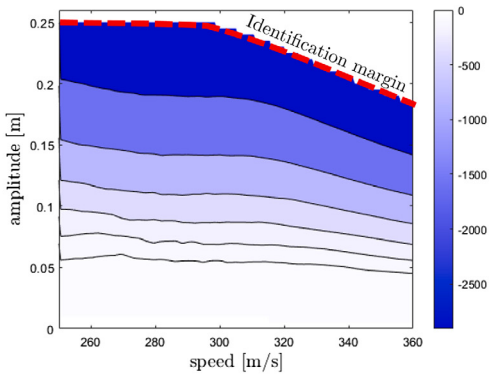

(b) Dissipated energy map by the sloshing forces

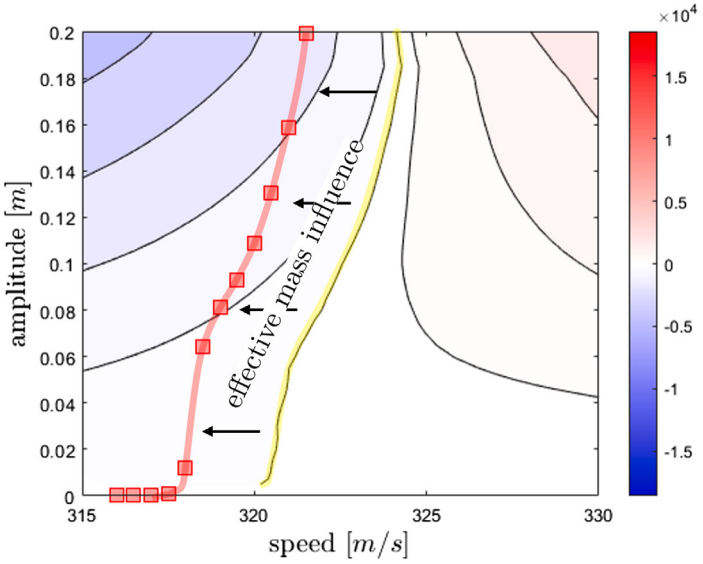

(c) Energy map of the full integrated system (with the LCOs)

Fig. 18. Energy maps.

$$b_n = \frac{M_{ac}}{2}\,\mathbf{i}_3 \cdot \boldsymbol{\psi}_n(\mathbf{x}_{lg}) - \iiint_V \rho_m\,\mathbf{i}_3 \cdot \boldsymbol{\psi}_n\,\mathrm{d}V \tag{22}$$

where $M_{ac}/2$ is the aircraft half mass, $\mathbf{x}_{lg}$ is the position of the landing gear, ρ_m is the material density, and V is the material volume. The first term in Eq. (22) represents the mutual force between the landing gear and the ground, whereas the second term is the fictitious force given by the deceleration of the wing reference system with respect to the ground.

The present simplified modelling is based on the following hypotheses: *i)* the vertical acceleration of the landing gear is assumed equal to the fuselage vertical acceleration; *ii)* there exists only a one way coupling between the dynamics of the fuselage and the wing dynamics; *iii)* ground effects and high-lift devices are not accounted. Using an operational landing acceleration measured at the fuselage of a typical aircraft, the analysis is conducted for the two models taken into account. Fig. 19(a) compares the wing tip response of the sloshing fuel model with the frozen fuel model. Slosh dynamics provides a bit more damped response with respect to the frozen fluid model. Moreover, Fig. 19(b) shows the response of the dynamic sloshing forces.

5. Conclusions

This work studied the effects of vertical sloshing dynamics of fuel inside the tanks on the aeroelastic response of a prototype wing when high vertical accelerations caused by the vibrations of the structure lead to the fragmentation of the fuel free surface. The fluid impacts generated on the tank ceiling are a source of damping for the overall structure that has hardly been considered before when computing the dynamic loads of the wings.

More specifically, a hybrid modelling was used to predict the aeroelastic/sloshing response. The coefficients of the aeroelastic model were obtained by a standard linear aeroelastic solver whilst a data-driven approach was used to obtain slosh dynamics which were subsequently incorporated into the aeroelastic framework. The vertical sloshing dynamics was considered using neural networks trained with experimental data from a scaled tank introduced in Ref. [17]. The neural-network based ROM was properly scaled for being integrated into the aeroelastic system considering the current tank dimensions.

The results concerned the damping performance under pre-critical conditions as well as the limit cycle oscillation caused by the sloshing. In fact, sloshing is the only nonlinear phenomenon modelled in the present work and has proven to be effective in

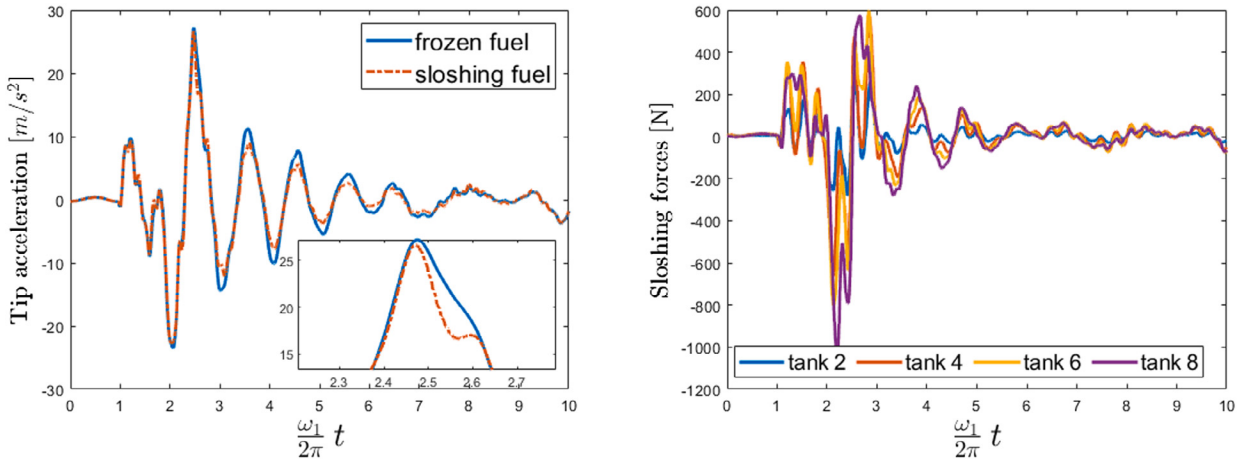

(a) Tip vertical acceleration (b) Dynamic sloshing forces

Fig. 19. Landing response analysis.

providing an additional margin of stability in post-critical conditions. Finally, the effect of sloshing in aircraft landing was also investigated showing the increased damping of the structural response.

Declaration of competing interest

The authors declare that they have no known competing financial interests or personal relationships that could have appeared to influence the work reported in this paper.

Acknowledgements

This paper has been supported by SLOWD project. The SLOWD project has received funding from the European Union's Horizon 2020 research and innovation programme under grant agreement No. 815044.

Appendix A. Interpretation of the non-dimensional dissipated energy and sloshing-effective mass fraction

In vertical simply harmonic motion, the response of a nonlinear system provides a nonlinear sloshing force such that its Fourier transform is not uniquely defined as a simple spectral line. However, filtering the response about the excitation frequency preserves the most of the signal properties and can be used here to interpret the role and the origin of the dissipate energy and effective mass.

Let's suppose that, given the amplitude of the motion a and the frequency Ω, it is possible to linearise the dynamic sloshing force by assuming:

$$\Delta f_{S_z} \cong -\beta(\Omega,a)m_l\ddot{u}_z - \gamma(\Omega,a)\dot{u}_z \tag{A.1}$$

where $\beta(\Omega,a)m_l$ is an incremental term with respect to the frozen fluid model and $\gamma(\Omega,a)$ is a quantity that provides the dependency of the sloshing force with respect to the input velocity. Both β and γ generally depend on the frequency and amplitude of the motion.

Assuming a steady generalised harmonic input for u_z like $\check{u}_z = ae^{j\Omega t}$ and a consequent generalised expected harmonic output $\Delta\check{f}_{S_z} = Fe^{j(\Omega t+\varphi)}$, with F and φ, respectively the amplitude of the dynamic sloshing force and phase shift with respect to the tank motion, one has (see (A.1)):

$$\Delta\check{f}_{S_z} = -\Big(-\beta(\Omega,a)m_l\Omega^2 + \gamma(\Omega,a)j\Omega\Big)\check{u}_z \tag{A.2}$$

Thus, Eq. (A.2) yields

$$\frac{\Delta\check{f}_{S_z}}{m_l\Omega^2\check{u}_z} = \beta(\Omega,a) - j\frac{\gamma(\Omega,a)}{m_l\Omega} \tag{A.3}$$

$$\frac{\Delta\check{f}_{S_z}}{\Omega\check{u}_z} = \beta(\Omega,a)m_l\Omega - j\gamma(\Omega,a) \tag{A.4}$$

By taking the real and imaginary parts of Eqs. (A.3) and (A.4), one obtains

$$\beta(\Omega,a) = \frac{F}{m_l\,\Omega^2\,a}\cos(\varphi) = \Re\Big[\frac{\Delta\check{f}_{S_z}}{m_l\,\Omega^2\,\check{u}_z}\Big] \tag{A.5}$$

$$\gamma(\Omega,a) = -\frac{F}{\Omega\,a}\sin(\varphi) = -\Im\Big[\frac{\Delta\check{f}_{S_z}}{\Omega\,\check{u}_z}\Big] \tag{A.6}$$

A Fourier transform of the sloshing forces $\Delta\tilde{f}_{S_z}(\Omega)$, as well as the vertical tank motion $\tilde{u}_z(\Omega)$ at the excitation frequency Ω, can be used instead of the phasors for experimentally measured harmonic signals.

The dynamic sloshing force Δf_{S_z} can be expressed also as a function of the relative acceleration $\Delta\ddot{u}_{z_{l_G}}$ of the fluid centre of mass with respect to tank as $\Delta f_{S_z} = -m_l\Delta\ddot{u}_{z_{l_G}}$.[2] The motion of

[2] Indeed, assuming $\mathbf{u}_l$ the displacement field of the fluid continuum and $\mathbf{T}$ the stress tensor, the Cauchy momentum (conservation) equation projected in vertical direction $\mathbf{i}_3$ provides

$$\left[\iiint_V \rho\frac{D^2\mathbf{u}_l}{Dt^2}\mathrm{d}V - \iiint_V \mathrm{div}\mathbf{T}\mathrm{d}V - g\iiint_V \rho\mathbf{i}_3\mathrm{d}V\right]\cdot\mathbf{i}_3 = 0 \tag{A.7}$$

Assuming $\mathbf{u}_l = u_z\mathbf{i}_3 + \Delta\mathbf{u}_l$, being u_z the vertical displacement of the tank and $\Delta\mathbf{u}_l$ the relative displacement of each fluid point of the domain, and using the divergence theorem, one has:

$$m_l\ddot{u}_z + \iiint_V \rho\frac{D^2\Delta\mathbf{u}_l}{Dt^2}\mathrm{d}V = -f_{S_z} + m_l g \tag{A.8}$$

Neglecting the hydrostatic contribution and considering the dynamic sloshing force given by $\Delta f_{S_z} = f_{S_z} + m_l\ddot{u}_z$, it is possible to obtain:

$$\Delta f_{S_z} = -m_l\Delta\ddot{u}_{z_{l_G}} \tag{A.9}$$

that is, the dynamic sloshing forces depend on the relative motion of the fluid centre of mass.

the fluid centre of mass is therefore given by $\Delta u_{z_{l_G}} = a_l e^{j(\Omega t+\varphi)}$ where $a_l = F/(m_l\Omega^2)$ is the amplitude of the relative motion of the fluid centre of mass with respect to the tank. This way, it is possible to recast the sloshing effective mass variation ratio as:

$$\beta(\Omega, a) = \Re\left[\frac{\Delta\check{u}_{z_{l_G}}(\Omega)}{\check{u}_z(\Omega)}\right] = \frac{a_l}{a}\cos(\varphi) \tag{A.10}$$

Thus, the variation of the sloshing-effective mass assumes the meaning of the ratio between the amplitude of the phased relative motion of the fluid centre of mass and the tank motion amplitude. The identified $\beta(\Omega, a)$ in Fig. 5(b) results to be negative throughout the interest frequency-amplitude domain. Therefore, the relative motion of fluid centre of mass is always counter-phased with respect to the tank.

On the other hand, from Eq. (A.6), can be demonstrated that:

$$\Phi_d(\Omega, a) = \frac{\pi\gamma}{m_l\Omega} = -\frac{\pi F}{m_l\Omega^2 a}\sin(\varphi) = \pi\frac{a_l}{a}\sin(\varphi) \tag{A.11}$$

From Eqs. (A.10) and (A.11), we can estimate the relative amplitude and phase shift of the fluid centre of mass displacement from which we can interpret the role of dissipated energy and effective mass.

References

[1] F. Gambioli, A. Chamos, S. Jones, P. Guthrie, J. Webb, J. Levenhagen, P. Behruzi, F. Mastroddi, A. Malan, S. Longshaw, J. Cooper, L. Gonzalez, S. Marrone, Sloshing wing dynamics – project overview sloshing wing dynamics – project overview, in: Proceedings of 8th Transport Research Arena TRA 2020, 2020.

[2] R.D. Firouz-Abadi, P. Zarifian, H. Haddadpour, Effect of fuel sloshing in the external tank on the flutter of subsonic wings, J. Aerosp. Eng. 27 (5) (2014) 04014021.

[3] Charbel Farhat, Edmond Kwan-yu Chiu, David Amsallem, Jean-Sébastien Schotté, Roger Ohayon, Modeling of fuel sloshing and its physical effects on flutter, AIAA J. 51 (9) (2013) 2252–2265.

[4] Marta Colella, Francesco Saltari, Marco Pizzoli, Franco Mastroddi, Sloshing reduced-order models for aeroelastic analyses of innovative aircraft configurations, Aerosp. Sci. Technol. 118 (2021) 107075.

[5] James Hall, T. Rendall, Christian B. Allen, A two-dimensional computational model of fuel sloshing effects on aeroelastic behaviour, in: 31st AIAA Applied Aerodynamics Conference, 2013.

[6] J. Hall, T.C.S. Rendall, C.B. Allen, H. Peel, A multi-physics computational model of fuel sloshing effects on aeroelastic behaviour, J. Fluids Struct. 56 (2015) 11–32.

[7] Thomas Brooke Benjamin, Fritz Joseph Ursell, Geoffrey Ingram Taylor, The stability of the plane free surface of a liquid in vertical periodic motion, Proc. R. Soc. Lond. Ser. A, Math. Phys. Sci. 225 (1163) (1954) 505–515.

[8] Francesco Gambioli, Roberto Alegre Usach, Thomas Wilson, Philipp Behruzi, Experimental evaluation of fuel sloshing effects on wing dynamics, in: 18th Int. Forum Aeroelasticity Struct. Dyn. IFASD 2019, 2019.

[9] Branislav Titurus, Jonathan E. Cooper, Francesco Saltari, Franco Mastroddi, Francesco Gambioli, Analysis of a sloshing beam experiment, in: International Forum on Aeroelasticity and Structural Dynamics, Savannah, Georgia, USA, vol. 139, 2019.

[10] Francesco Saltari, Marco Pizzoli, Giuliano Coppotelli, Francesco Gambioli, Jonathan E. Cooper, Franco Mastroddi, Experimental characterisation of sloshing tank dissipative behaviour in vertical harmonic excitation, J. Fluids Struct. 109 (2022) 103478.

[11] Joe J. De Courcy, Lucian Constantin, Branislav Titurus, T. Rendall, Jonathan E. Cooper, Gust loads alleviation using sloshing fuel, in: AIAA Scitech 2021 Forum, 2021.

[12] E. Graham, A.M. Rodriquez, The characteristics of fuel motion which affect airplane dynamics, Technical report, Douglas Aircraft Co. Inc., Defense Technical Information Center, 1951.

[13] H. Norman Abramson, The dynamic behaviour of liquids in moving containers with applications to space vehicle technology, Natl. Aeronaut. Space Adm. (1966) 464.

[14] Jean-Sébastien Schotté, Roger Ohayon, Various modelling levels to represent internal liquid behaviour in the vibration analysis of complex structures, Comput. Methods Appl. Mech. Eng. 198 (21) (2009) 1913–1925.

[15] Francesco Saltari, Alessandro Traini, Francesco Gambioli, Franco Mastroddi, A linearized reduced-order model approach for sloshing to be used for aerospace design, Aerosp. Sci. Technol. 108 (2021) 106369.

[16] Marco Pizzoli, Francesco Saltari, Franco Mastroddi, Jon Martinez-Carrascal, Leo M. González-Gutiérrez, Nonlinear reduced-order model for vertical sloshing by employing neural networks, in: Nonlinear Dynamics, 2021.

[17] Marco Pizzoli, Francesco Saltari, Giuliano Coppotelli, Franco Mastroddi, Experimental validation of neural-network-based nonlinear reduced-order model for vertical sloshing, in: AIAA Scitech 2022 Forum, 2022.

[18] Andrea Mannarino, Paolo Mantegazza, Nonlinear aeroelastic reduced order modeling by recurrent neural networks, J. Fluids Struct. 48 (2014) 103–121.

[19] Simon O. Haykin, Neural Networks and Learning Machines, 3 edition, Pearson, 2009.

[20] E. Albano, W.P. Rodden, Msc/nastran aeroelastic analysis' user's guide, in: MSC Software, 1994.

[21] Mordechay Karpel, Design for active flutter suppression and gust alleviation using state-space aeroelastic modeling, J. Aircr. 19 (3) (1982) 221–227.

[22] L. Morino, F. Mastroddi, R. De Troia, G.L. Ghiringhelli, P. Mantegazza, Matrix fraction approach for finite-state aerodynamic modeling, AIAA J. 33 (4) (1995) 703–711.

[23] James Reese, Some effects of fluid in pylon-mounted tanks on flutter, Technical report, National Advisory Committee for Aeronautics, 07 1955.

[24] John Sewall, An experimental and theoretical study of the effect of fuel on pitching-translation flutter, Technical report, National Advisory Committee for Aeronautics, 12 1955.

[25] Jon Martínez-Carrascal, Leo González-Gutiérrez, Experimental study of the liquid damping effects on a sdof vertical sloshing tank, J. Fluids Struct. 100 (2021) 103172.

[26] L. Constantin, J. De Courcy, B. Titurus, T.C.S. Rendall, J.E. Cooper, Analysis of damping from vertical sloshing in a sdof system, Mech. Syst. Signal Process. 152 (2021) 107452.

[27] Byron S. Sykes, Arnaud G. Malan, Francesco Gambioli, Novel nonlinear fuel slosh surrogate reduced-order model for aircraft loads prediction, J. Aircr. 55 (3) (2018) 1004–1013.

[28] Oliver Nelles, Nonlinear System Identification, from Classical Approaches to Neural Networks, Fuzzy Models, and Gaussian Processes, 2 edition, Springer, 2021.

[29] Mark Hudson Beale, Martin T. Hagan, Howard B. Demuth, Deep Learning Toolbox, Mathworks, r2020a edition, 2020.

[30] J. Calderon-Sanchez, J. Martinez-Carrascal, L.M. Gonzalez-Gutierrez, A. Colagrossi, A global analysis of a coupled violent vertical sloshing problem using an sph methodology, Eng. Appl. Comput. Fluid Mech. 15 (1) (2021) 865–888.

[31] Karthik Menon, Rajat Mittal, Aeroelastic response of an airfoil to gusts: prediction and control strategies from computed energy maps, J. Fluids Struct. 97 (2020) 103078.